Chaos, Solitons and Fractals 200 (2025) 116995

Contents lists available at ScienceDirect

Chaos, Solitons and Fractals

journal homepage: www.elsevier.com/locate/chaos

Effect of orbital angular momentum on photonic spin Hall effect in a rovibrational optical cavity

Muqaddar Abbas [a], Ghaisud Din [a], Akhtar Munir [b], Hamid R. Hamedi [c,*], Pei Zhang [a,*]

[a] Ministry of Education Key Laboratory for Nonequilibrium Synthesis and Modulation of Condensed Matter, Shaanxi Province Key Laboratory of Quantum Information and Quantum Optoelectronic Devices, School of Physics, Xi'an Jiaotong University, Xi'an, 710049, China
[b] Department of Physics, University of Shanghai for Science and Technology, Shanghai 200093, China
[c] Institute of Theoretical Physics and Astronomy, Vilnius University, Sauletekio 3, Vilnius LT-10257, Lithuania

ARTICLE INFO

Keywords:
Rovibrational cavity
Laguerre–Gaussian beam
Photonic spin Hall effect
Orbital angular momentum

ABSTRACT

We investigate the influence of orbital angular momentum (OAM) on the optical response of an intracavity rovibrational optomechanical system interacting with a weak probe field. In the absence of OAM, the system exhibits a well-resolved optomechanically induced transparency (OMIT) window at zero detuning, accompanied by strong photonic spin Hall effect (SHE) shifts. Introducing non-zero OAM activates rotational degrees of freedom, leading to rovibrational mode hybridization and the emergence of multiple transparency dips in the absorption spectrum. As the OAM increases, the absorption profile evolves from a single window to multiple split and broadened transparency regions, indicating strengthened coupling between rotational and vibrational modes. However, the photonic SHE response does not scale monotonically with OAM. While low OAM values degrade the photonic SHE due to dispersion flattening and phase gradient suppression, higher OAM values can recover or even amplify the spin-dependent shift under specific detuning conditions. This recovery stems from enhanced hybridization and sharper phase gradients near broadened transparency windows. Density plots of the photonic SHE shift versus OAM and incidence angle reveal a nontrivial interplay between light's angular momentum and the spin–orbit interaction, showing that field localization, detuning, and phase dispersion jointly govern the system's light-steering capabilities. Notably, the probe field starts and ends as a Gaussian beam, and OAM is introduced parametrically via cavity-mediated interaction and not through a vortex phase front imposed on the input beam. Thus, the reflected intensity distribution remains Gaussian-shaped, but its centroid (spin-dependent) is influenced by the OAM-controlled changes that lead to a modified photonic SHE shift. These findings highlight the tunability of intracavity optomechanical systems via OAM for applications in optical sensing, spin-controlled photonics, and structured light–matter interactions.

1. Introduction

Electromagnetically induced transparency (EIT) is a quantum optical phenomenon in which the application of a strong control (pump) field to an atomic system creates destructive interference between excitation pathways. This interference suppresses the absorption of a weak probe field, resulting in the emergence of a narrow transparency window [1]. A closely related effect, known

* Corresponding authors.
E-mail addresses: hamid.hamedi@tfai.vu.lt (H.R. Hamedi), zhangpei@mail.ustc.edu.cn (P. Zhang).

https://doi.org/10.1016/j.chaos.2025.116995
Received 2 June 2025; Received in revised form 27 July 2025; Accepted 1 August 2025
Available online 14 August 2025

as optomechanically induced transparency (OMIT), occurs in cavity optomechanical systems and stems from interference between optical and mechanical excitation pathways. Specifically, OMIT results from the coherent interaction between an optical cavity mode and the mechanical vibrations (phonon modes) of a movable mirror or membrane [2,3].

Cavity optomechanics has emerged as a powerful framework for exploring quantum-level interactions between electromagnetic fields and mechanical degrees of freedom. The field has witnessed substantial progress, encompassing both rigorous theoretical models and high-precision experimental implementations [4–7]. Among the key phenomena investigated in this domain is OMIT, which was first proposed theoretically and later validated through experiments in platforms ranging from microscale cavities to nanoscale mechanical resonators [8–12].

A notable characteristic of OMIT systems is their ability to manipulate the group velocity of light, enabling both subluminal and superluminal propagation. These effects have important implications for technologies such as optical delay lines, information buffering, and high-precision metrology [12]. Furthermore, the coherent coupling between optical and mechanical modes paves the way for quantum memory applications, in which mechanical motion can be used to reversibly store and retrieve quantum states of light in a noise-resilient manner [13–17].

Recent advancements in optomechanics have introduced an intriguing class of systems that exploit Laguerre–Gaussian (LG) cavity modes, which are distinguished by their helical phase fronts and quantized orbital angular momentum (OAM). A particularly compelling configuration features an optical cavity composed of one fixed mirror and one mechanically rotatable mirror, allowing for the exchange of OAM between the intracavity optical field and the rotational motion of the mirror [18]. In these systems, the cavity modes inherently exhibit a helical phase structure, and the interaction is mediated by spiral phase elements that serve as OAM converters, thereby exerting a torque on the rotating mirror.

These OAM-coupled optomechanical platforms have gained considerable attention due to their capability to support light–matter interactions that are sensitive to angular momentum degrees of freedom. Noteworthy studies have shown the emergence of quantum entanglement between the LG light field and the rotational motion of the mirror, offering new avenues for encoding quantum information in angular momentum states [19,20]. Moreover, systems incorporating both rotational and vibrational mechanical modes exhibit hybrid entanglement dynamics, wherein the exchange of energy and information occurs simultaneously across multiple degrees of freedom [21].

In addition to their quantum properties, the optical and mechanical stability of LG-based cavities has been systematically investigated. Using the transfer matrix method in the context of ray optics, researchers have analyzed the stability conditions of systems incorporating spiral phase plates, highlighting how rotational symmetry and OAM conservation influence the cavity's eigenmode structure and alignment tolerances [22]. Collectively, these LG rotational cavities offer a versatile platform for studying structured light–matter interactions, with promising applications in quantum sensing, angular momentum-based photonic devices, and fundamental investigations of optomechanical torque.

An intriguing manifestation of light–matter interaction governed by spin–orbit coupling is the photonic spin Hall effect (SHE), a cornerstone in the emerging field of spin photonics. Analogous to the electronic SHE, where spin-polarized electrons experience transverse deflection under an applied electric potential gradient [23]—the photonic SHE manifests as a spin-dependent transverse shift of light, in which left-circularly polarized (LCP) and right-circularly polarized (RCP) components of an optical beam are spatially separated due to spin–orbit interaction. This splitting arises from spatially varying refractive index profiles or material interfaces, which act as effective potentials for spin photons [24,25].

Originally proposed by Onoda et al. in 2004 [24] and further developed through a rigorous theoretical framework by Bliokh and Bliokh [25], the photonic SHE has since become a focal point in structured light studies. A milestone in its experimental realization was achieved by Hosten and Kwiat in 2008, who employed weak measurement techniques to resolve the minute spin-dependent beam shifts that characterize this phenomenon [26]. Fundamentally, the photonic SHE stems from the spin–orbit interaction of light, ensuring angular momentum conservation as the intrinsic (spin) and extrinsic (orbital) components of light redistribute during reflection or refraction processes [27,28].

To improve the detectability and enhance the sensitivity of the photonic SHE, a variety of advanced techniques have been explored. Among these, the weak value amplification (WVA) methodology has emerged as a particularly powerful approach, capable of significantly amplifying the transverse displacement between spin-polarized components. This enhancement has facilitated ultra-precise optical metrology and sensing applications [29,30]. Nevertheless, conventional photonic platforms typically suffer from limited tunability and lack the real-time dynamic control required for tailoring spin-dependent beam shifts across variable optical environments. These inherent constraints have catalyzed growing interest in reconfigurable architectures and cavity-enhanced systems, which can substantially boost and manipulate the photonic SHE via engineered light–matter interaction schemes. In this context, the photonic SHE has garnered widespread attention due to its capacity to control spin-resolved photon transport in a broad array of physical platforms, including plasmonic metasurfaces [31], photonic crystal structures [32], atomic ensemble-based systems [33–35], and hybrid cavity magnomechanical interfaces [36].

Although significant progress has been made in understanding intracavity rovibrational interactions, particularly through studies of OMIT and mode hybridization, the role of spin-dependent light–matter effects in such systems remains largely unexplored. In particular, the photonic SHE, a hallmark of spin–orbit coupling in structured light, has not been comprehensively investigated within intracavity platforms driven by OAM. In this work, we address this gap by examining the interplay between OAM and spin–orbit interactions in a rovibrational optomechanical cavity. By incorporating LG modes with tunable OAM, we systematically investigate how rotational degrees of freedom affect probe field transmission, phase dispersion, and the resulting spin-dependent beam shifts characteristic of the photonic SHE. Crucially, the probe field enters and exits the cavity as a Gaussian beam, with OAM imparted parametrically through cavity-mediated interactions rather than through an imposed vortex phase front. As a result, the reflected

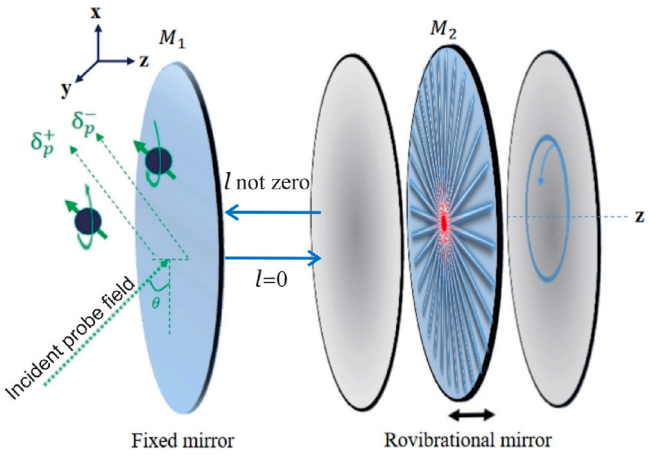

Fig. 1. Schematic representation of the rovibrational optomechanical cavity system. The cavity consists of a fixed mirror and a movable mirror, the latter supporting both vibrational and rotational mechanical modes. The system is simultaneously driven by a weak probe field and a strong control field, each characterized by its own amplitude and frequency.

beam retains a Gaussian intensity profile, while its centroid exhibits spin-dependent displacements governed by OAM-controlled modifications to the intracavity dynamics. Our findings show that OAM-induced hybridization between rotational and vibrational modes leads to pronounced changes in both the absorption spectrum and the spin-dependent spatial shift of the reflected beam. This study not only advances the understanding of spin–orbit coupling in hybrid optomechanical systems but also introduces a reconfigurable platform for tuning the photonic SHE via OAM, with promising applications in spin controlled light routing, precision metrology, and structured light based photonic technologies.

2. Proposed model

2.1. Theoretical modeling of the photonic spin hall effect

The physical setup is depicted in Fig. 1, which represents a rovibrational cavity consisting of a fixed mirror M_1 and a movable mirror M_2. The cavity supports a single quantized optical mode with frequency ω_c, and has an overall cavity length L. The fixed mirror M_1 is partially transmitting, allowing the injection of an incident probe field composed of RCP and LCP, respectively.

The movable mirror M_2, located at the opposite end of the cavity, is modeled as a quantum mechanical oscillator that supports both vibrational and rotational degrees of freedom—collectively referred to as rovibrational modes. These internal mechanical modes interact with the intracavity optical field via radiation pressure.

The cavity is driven simultaneously by a strong control field and a weak probe field, each with its own frequency and amplitude. The radiation pressure exerted by the optical field on the movable mirror induces optomechanical coupling, which modulates the intracavity dynamics. This configuration provides a robust platform for studying the transfer of optical angular momentum to mechanical motion and for investigating the interplay between light and rovibrational excitations in an optomechanical framework.

To determine the reflection characteristics of a three-layer optical cavity for both transverse magnetic (TM) and transverse electric (TE) polarization modes, we employ the transfer matrix formalism. Each layer in the multilayered structure is associated with a characteristic transfer matrix, which encapsulates the wave propagation and boundary conditions within that layer. The transfer matrix corresponding to the ith layer is formulated as [37,38]

$$\mathcal{M}_i(k_x,\omega_p,d_i)=\begin{pmatrix}\cos(k_z^i d_i) & \frac{i\sin(k_z^i d_i)}{q_{is}}\\ iq_{is}\sin(k_z^i d_i) & \cos(k_z^i d_i)\end{pmatrix}, \tag{1}$$

where $k_z^i=\sqrt{\epsilon_i k^2-k^2\sin^2\theta}$ represents the longitudinal component of the wave vector in the ith medium of thickness d_i, and q_{is} denotes the corresponding effective wave impedance term. The cumulative optical response of the entire layered system is captured by the total transfer matrix, constructed as the ordered product of the individual matrices:

$$Y(k_x,\omega_p)=\mathcal{M}_1(k_x,\omega_p,d_1)\mathcal{M}_2(k_x,\omega_p,d_2)\mathcal{M}_3(k_x,\omega_p,d_3). \tag{2}$$

This matrix formalism allows for precise calculation of the reflection coefficients R_p and R_s for TM and TE polarized waves, respectively, enabling a comprehensive analysis of polarization-dependent optical behavior in stratified media.

The reflection coefficients corresponding to TE and TM polarized light in a multilayer structure can be determined using the elements of the total transfer matrix $Y(k_x,\omega_p)$. For TE (or s-polarized) waves, the reflection coefficient is expressed as:

$$R_s=\frac{q_{1s}(y_{11}+y_{12}q_{3s})-(q_{3s}y_{22}+y_{21})}{q_{1s}(y_{11}+y_{12}q_{3s})+(q_{3s}y_{22}+y_{21})}, \tag{3}$$

where q_{1s} and q_{3s} represent the effective transverse wave impedances in the first and third layers, respectively, and y_{ij} denotes the components of the overall transfer matrix. For TM (or p-polarized) waves, the reflection coefficient can be derived by replacing q_{is} with p_{im}, where $p_{im} = q_{is}/\epsilon_i$:

$$R_p = \frac{p_{1m}(y_{11} + y_{12}p_{3m}) - (p_{3m}y_{22} + y_{21})}{p_{1m}(y_{11} + y_{12}p_{3m}) + (p_{3m}y_{22} + y_{21})}. \tag{4}$$

To analyze the photonic SHE, we consider a reflected Gaussian beam decomposed into its RCP and LCP components. The corresponding field amplitudes at the reflection plane (x_r, y_r, z_r) are given by:

$$\mathcal{E}_r^{\pm}(x_r, y_r, z_r) = \frac{\omega_0}{\omega} \exp\left[-\frac{x_r^2 + y_r^2}{\omega}\right] \times \left[R_p - \frac{2ix_r}{k\omega}\frac{\partial R_p}{\partial \theta} \mp \frac{2y_r \cot\theta}{k\omega}(R_s + R_p)\right] \tag{5}$$

where ω_0 is the beam waist, ω is the beam width at the interface, and k is the wave number in the incident medium.

The transverse spin-dependent displacement associated with photonic SHE is calculated from the centroid of the reflected intensity distribution for each circular polarization component:

$$\delta_p^{\pm} = \frac{\int y|\mathcal{E}_r^{\pm}(x_r, y_r, z_r)|^2 \, dx_r dy_r}{\int |\mathcal{E}_r^{\pm}(x_r, y_r, z_r)|^2 \, dx_r dy_r}. \tag{6}$$

By carrying out the integration analytically, one obtains an explicit expression for the spin-dependent shift [39–41]:

$$\delta_p^{\pm} = \mp \frac{k_1 \omega_0^2 \mathrm{Re}\left[1 + \frac{R_s}{R_p}\right]\cot\theta}{k_1^2\omega_0^2 + \left|\frac{\partial \ln R_p}{\partial \theta}\right|^2 + \left|\left(1 + \frac{R_s}{R_p}\right)\cot\theta\right|^2}, \tag{7}$$

where δ_p^+ corresponds to RCP photonic SHE shift, and δ_p^- to LCP photonic SHE shift, with both exhibiting equal magnitudes but opposite directions.

In this analysis, the permittivities of the cavity boundaries (ϵ_1 and ϵ_3) are fixed, while the optical response of the intermediate cavity layer is dynamically linked to the quadratures of output probe field E_T through the relation $\epsilon_2 = 1 + E_T$. Here the quadratures of the output probe field E_T can be expressed as $E_T = u_p + iv_p$, where u_p and v_p denote the in-phase and out-of-phase quadratures, respectively. These components characterize the absorptive (u_p) and dispersive (v_p) response of the probe field as it interacts with the cavity [2,42].

Given that both R_s, R_p, and the photonic SHE displacement $\delta_p^{\pm}$ are inherently dependent on the tunability of ϵ_2, and consequently on E_T. We proceed to compute the output field related to the intracavity field through E_T using the quantum Langevin formalism.

2.2. Mathematical modeling of rovibrational cavity system

The total Hamiltonian governing the system dynamics is expressed as [43]

$$H = \hbar\Delta_a a^\dagger a + \frac{L_z^2}{2I_m} + \frac{1}{2}I_m\omega_\phi^2\phi^2 + \frac{P^2}{2m} + \frac{1}{2}m\omega_m^2 x^2 + \hbar g_\phi a^\dagger a\phi - \hbar g_{mc} a^\dagger a x + i\hbar E_l(a^\dagger - a) + i\hbar E_p(a^\dagger e^{-i\delta t} - a e^{i\delta t}). \tag{8}$$

In the above expression, the first term represents the free energy of the optical cavity mode, where a and $a^\dagger$ denote the annihilation and creation operators, respectively. The next two terms capture the rotational degrees of freedom: L_z is the angular momentum, I_m is the moment of inertia, ϕ is the angular displacement, and ω_ϕ is the associated angular frequency. The fourth and fifth terms describe the translational (vibrational) motion of the mirror, with P being its linear momentum, m the mirror mass, x the displacement, and ω_m the vibrational frequency.

The sixth term of the Hamiltonian encompasses interaction term that couples the cavity photons with the rotational motion, where $g_\phi = \frac{c\ell}{L}$ quantifies the strength of the rotation-cavity coupling, with ℓ being the OAM quantum number and L the cavity length. The seventh interaction term describes the radiation pressure coupling between the optical mode and the mechanical mirror displacement, governed by the coupling rate g_{mc}.

Finally, the last two terms represents the coherent driving of the cavity by an external control field (with amplitude E_l) and a weak probe field (with amplitude E_p and detuning δ), both interacting with the cavity mode through standard input–output processes.

Applying the Heisenberg formalism to the system operators and incorporating both dissipation and quantum noise sources, the corresponding quantum Langevin equations can be derived as:

$$\dot{a} = -(\mathrm{i}\Delta_a + \kappa)a + \mathrm{i}g_\phi a\phi - \mathrm{i}g_{mc}ax + E_l + E_p e^{-\mathrm{i}\delta t} + \sqrt{2\kappa}a_{\mathrm{in}},$$

$$\dot{\phi} = \frac{L_z}{I_m},$$

$$\dot{L}_z = -I_m\omega_\phi^2\phi + \hbar g_\phi a^\dagger a - \gamma_\phi L_z,$$

$$\dot{x} = \frac{P}{m},$$

$$\dot{P} = -m\omega_m^2 x - \hbar g_{mc} a^\dagger a - \gamma_m P. \tag{9}$$

In these equations, the field operator a evolves under the influence of cavity decay rate κ, optical drives E_l and E_p, and coupling to both rotational (ϕ) and mechanical (x) degrees of freedom. The input vacuum fluctuations $a_{\text{in}}(t)$ enter through the coupling mirror, characterized by κ, and satisfy the commutation relation $\langle a_{\text{in}}(t) a_{\text{in}}^\dagger(t')\rangle = \delta(t-t')$, assuming $\langle a_{\text{in}}(t)\rangle = 0$. These quantum noise terms play a crucial role in determining the dynamical and steady-state behavior of the intracavity field [44,45].

In addition, the steady-state solution together with small fluctuations about these values can be expressed as

$$a = \alpha + \delta a, \quad \phi = \phi_s + \delta\phi, \quad x = x_s + \delta x. \tag{10}$$

Starting from Eq. (9), the equations governing the fluctuation operators take the form

$$\begin{aligned}\delta\dot{a} = &-(\mathrm{i}\Delta_a + \kappa)\delta a + \mathrm{i}g_\phi(\alpha\delta\phi + \phi_s\delta a) + E_l \\ &- \mathrm{i}g_{mc}(\alpha\delta x + x_s\delta a) + E_p e^{-\mathrm{i}\delta t},\end{aligned} \tag{11}$$

$$\delta\dot{\phi} = \frac{\delta L_z}{I_m}, \tag{12}$$

$$\delta\dot{L}_z = -I_m\omega_\phi^2\delta\phi + \hbar g_\phi(\alpha^*\delta a + \alpha\delta a^*) - \gamma_\phi\delta L_z, \tag{13}$$

$$\delta\dot{x} = \frac{\delta P}{m}, \tag{14}$$

$$\delta\dot{P} = -m\omega_m^2\delta x - \hbar g_{mc}(\alpha^*\delta a + \alpha\delta a^*) - \gamma_m\delta P. \tag{15}$$

Here, the steady-state quantities α, x_s, and ϕ_s are given by

$$\alpha = \frac{E_l}{\mathrm{i}\Delta + \kappa}, \tag{16}$$

$$x_s = \frac{\hbar g_{mc}|\alpha|^2}{m\omega_m^2}, \tag{17}$$

$$\phi_s = \frac{\hbar g_\phi|\alpha|^2}{I_m\omega_\phi^2}. \tag{18}$$

Where $\Delta = \Delta_a + g_{\text{mc}}x_s - g_\phi\phi_{\text{s}}$ is the effective detuning. To investigate the response of the probe field, we apply the ansatz

$$\delta a = \delta a_- e^{-\mathrm{i}\delta t} + \delta a_+ e^{\mathrm{i}\delta t}, \tag{19}$$

$$\delta\phi = \delta\phi_- e^{-\mathrm{i}\delta t} + \delta\phi_+ e^{\mathrm{i}\delta t}, \tag{20}$$

$$\delta L_z = \delta L_{z,-} e^{-\mathrm{i}\delta t} + \delta L_{z,+} e^{\mathrm{i}\delta t}, \tag{21}$$

$$\delta x = \delta x_- e^{-\mathrm{i}\delta t} + \delta x_+ e^{\mathrm{i}\delta t}. \tag{22}$$

Substituting these expressions into Eqs. (11)–(15) allows us to extract the output probe field component a_-. The characteristics of this output field are obtained by employing the input–output relation [42]:

$$E_{\text{out}}(t) + E_p e^{-\mathrm{i}\delta t} + E_l = \sqrt{2\kappa}a, \tag{23}$$

where the output field decomposes as

$$E_{\text{out}}(t) = E_{\text{out}}^{(0)} + E_{\text{out}}^{+} E_{p_i} e^{-\mathrm{i}\delta t} + E_{\text{out}}^{-} E_{p_i} e^{\mathrm{i}\delta t}. \tag{24}$$

Solving these relations yields

$$E_{\text{out}}^{+} = \frac{\sqrt{2\kappa}a_-}{E_p} - 1, \tag{25}$$

and equivalently,

$$E_{\text{out}}^{+} + 1 = \frac{\sqrt{2\kappa}a_-}{E_{p_i}} = E_T, \tag{26}$$

where the amplitude a_- can be written as the ratio

$$a_- = \frac{\mathcal{A}}{\mathcal{B}}, \tag{27}$$

with

$$\mathcal{A} = \mathrm{i}I_m m\left(\gamma_m\delta - \mathrm{i}(\delta-\omega_m)(\delta+\omega_m)\right)\left(\gamma_\phi\delta - \mathrm{i}(\delta-\omega_\phi)(\delta+\omega_\phi)\right)(\delta + \mathrm{i}\kappa + \Delta)$$

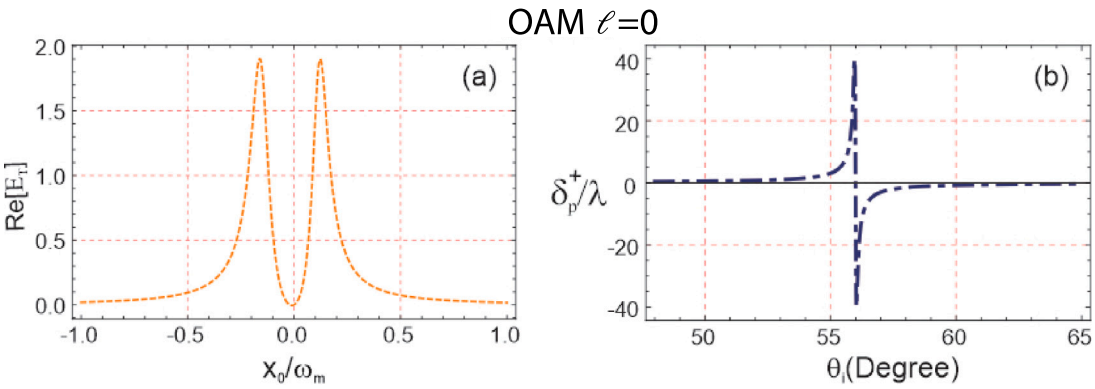

Fig. 2. (a) Absorption (dashed curve) characteristics of the intracavity rovibrational system as a function of the normalized probe field detuning x_0/ω_m. Scaling relation for the detuning parameter: $\delta = x_0\omega_m + \omega_m$. This scaling is used to define the zero reference point for $\delta = \omega_b$. The system parameters are: mechanical oscillator mass $m = 0.8 \times 10^{-6}$ kg, cavity length $L = 0.005$ m, radius of the rotating mirror $R = 0.16 \times 10^{-6}$ m, laser power $p_l = 6 \times 10^{-3}$ W, wavelength of probe field $\lambda = 22.7$ mm, optical decay rate $\kappa = \omega_\phi/10$, mechanical and rotational frequencies $\omega_m = 5.7 \times 10^6$ Hz and $\omega_\phi = 5.6 \times 10^6$ Hz, and dissipation rates $\gamma_\phi = \gamma_m = 0.00014$ Hz. The orbital angular momentum is fixed at $\ell = 0$ in this analysis. (b) Normalized photonic SHE shift δ_p^+/λ plotted as a function of the incident angle θ for a probe field detuning of $x_0 = -0.01\,\omega_m$ (blue dot–dashed line). The dielectric constants are $\epsilon_1 = \epsilon_3 = 2.22$ and $\epsilon_2 = 1 + E_T$, with mirror thicknesses $d_1 = 0.1 \times 10^{-3}$ m and $d_2 = 0.4 \times 10^{-3}$ m and beam waist $\omega_0 = 80\lambda$. As in the previous case, the orbital angular momentum is set to $\ell = 0$ throughout the analysis. (For interpretation of the references to color in this figure legend, the reader is referred to the web version of this article.)

$$+ \hbar|\alpha|^2 \left[g_\phi^2\, m \left(-\mathrm{i}\gamma_m\delta - \delta^2 + \omega_m^2\right) + g_{mc}^2 I_m \left(-\mathrm{i}\gamma_\phi\delta - \delta^2 + \omega_\phi^2\right)\right], \tag{28}$$

$$\begin{aligned}\mathcal{B} = {} & I_m m \left(\gamma_m\delta - \mathrm{i}(\delta - \omega_m)(\delta + \omega_m)\right)\left(\gamma_\phi\delta - \mathrm{i}(\delta - \omega_\phi)(\delta + \omega_\phi)\right)\left((\delta + \mathrm{i}\kappa)^2 - \Delta^2\right) \\ & + 2\hbar|\alpha|^2\Delta \left[g_\phi^2\, m \left(\mathrm{i}\gamma_m\delta + \delta^2 - \omega_m^2\right) + g_{mc}^2 I_m \left(\mathrm{i}\gamma_\phi\delta + \delta^2 - \omega_\phi^2\right)\right].\end{aligned} \tag{29}$$

The amplitude of the output field is related to the intracavity field through $E_T = \frac{\sqrt{2\kappa}a_-}{\mathcal{E}_p}$ [2].

3. Results and discussion

Fig. 2 illustrates the behavior of an intracavity rovibrational optomechanical system under the influence of a weak probe field, with OAM fixed at $\ell = 0$. This configuration effectively decouples the system from any rotational dynamics, allowing a clear examination of the vibrational optomechanical response alone.

Fig. 2(a) presents the absorption profile (dashed curve) as a function of the normalized probe detuning x_0/ω_m. The system parameters are: mechanical oscillator mass $m = 0.8 \times 10^{-6}$ kg, cavity length $L = 0.005$ m, radius of the rotating mirror $R = 0.16 \times 10^{-6}$ m, laser power $p_l = 6 \times 10^{-3}$ W, $g_\phi = \frac{c\,l}{L}$ (rotational cavity coupling strength), $\omega_c = 27.05$ MHz (Cavity frequency), $g_{mc} = \frac{\omega_c}{L}$ (Cavity–mechanical coupling). The wavelength $\lambda = 22.7$ mm, with an optical decay rate $\kappa = \omega_\phi/10$. The vibrational and rotational frequencies are $\omega_m = 5.7 \times 10^6$ Hz and $\omega_\phi = 5.6 \times 10^6$ Hz, respectively. Dissipation rates are kept minimal, with $\gamma_m = \gamma_\phi = 0.00014$ Hz.

In the absence of OAM ($\ell = 0$), the system transitions into a purely vibrational optomechanical regime, where the optical field couples solely to the mechanical vibrations of the cavity medium. This eliminates rotational perturbations and simplifies the interference dynamics that lead to OMIT. As shown in Fig. 2(a), a clear transparency window emerges at normalized detuning $x_0 \approx -0.01\,\omega_m$, resulting from destructive interference between the probe field and the anti-Stokes sideband generated via radiation pressure.

Fig. 2(b) shows the normalized photonic SHE shift δ_p^+/λ as a function of the incident angle θ for a fixed detuning $x_0 = -0.01\,\omega_m$ (blue dot–dashed line). The optical structure consists of three layers with permittivities $\epsilon_1 = \epsilon_3 = 2.22$, $\epsilon_2 = 1 + E_T$, and layer thicknesses $d_1 = 0.1 \times 10^{-3}$ m and $d_2 = 0.4 \times 10^{-3}$ m. Consistent with Fig. 2(a), the OAM is maintained at $\ell = 0$.

A pronounced spin-dependent beam displacement of nearly ± 40 is observed within the transparency window, driven by strong transverse index gradients induced by OMIT-enhanced dispersion. This enhancement arises from steep transverse phase gradients near the OMIT window, which induce strong spin–orbit interactions. The anisotropic cavity interface further differentiates the response of LCP and RCP, enabling a spin-dependent beam displacement. This decoupling of absorption and phase modulation highlights the dual functional capability of the system simultaneous OMIT and strong photonic SHE even without OAM.

This outcome reveals a noteworthy result: although the system exhibits minimal absorption due to OMIT, the transverse phase variation remains substantial enough to yield large photonic SHE shifts. The coexistence of low absorption and strong phase gradients underscores the dual utility of the vibrational optomechanical configuration in modulating both the intensity and trajectory of light. Therefore, Fig. 2 demonstrates that the $\ell = 0$ vibrational coupling regime supports a robust OMIT window and significant photonic SHE shifts, rendering this system attractive for tunable photonic devices, spin-controlled routing, and precision optical sensing.

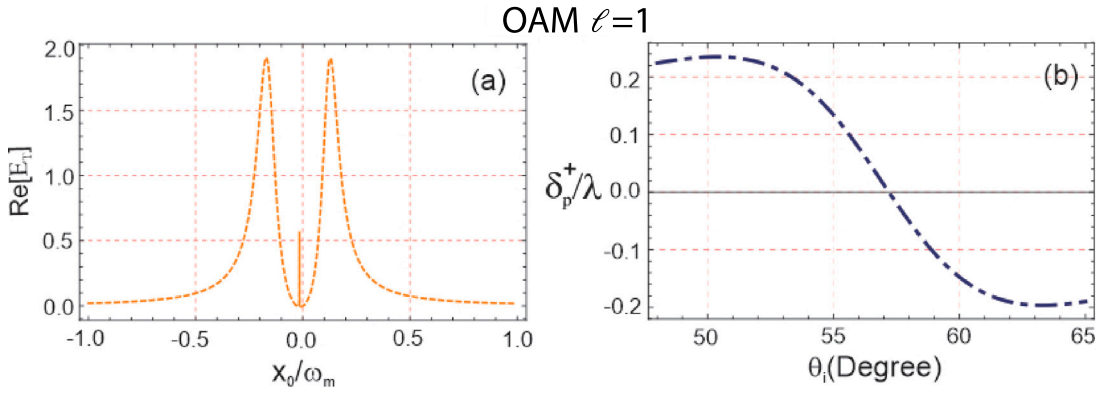

Fig. 3. (a) Absorption (dashed curve) characteristics of the intracavity rovibrational cavity system as functions of the normalized probe field detuning x_0/ω_m. Scaling relation for the detuning parameter: $\delta = x_0\omega_m + \omega_m$. This scaling is used to define the zero reference point for $\delta = \omega_b$. The parameters used are: mechanical oscillator mass $m = 0.8\times10^{-6}$ kg, cavity length $L = 0.005$ m, radius of the rotating mirror $R = 0.16\times10^{-6}$ m, laser power $p_l = 6\times10^{-3}$ W, wavelength of probe field $\lambda = 22.7$ mm, optical decay rate $\kappa = \omega_\phi/10$, mechanical and rotational frequencies $\omega_m = 5.7\times10^6$ Hz and $\omega_\phi = 5.6\times10^6$ Hz, and decay rates $\gamma_\phi = \gamma_m = 0.00014$ Hz. In all cases, the orbital angular momentum is set to $\ell = 1$. (b) Normalized photonic SHE shift δ_p^+/λ as a function of the incident angle θ for different probe field detunings. Here, the detuning is modified to $x_0 = -0.0415\,\omega_m$ (blue dot–dashed line), leading to a noticeable shift in the transparency window compared to the earlier case with $x_0 = -0.01\,\omega_m$. The other parameters remain unchanged: $\epsilon_1 = \epsilon_3 = 2.22$, $\epsilon_2 = 1 + E_T$, and mirror thicknesses $d_1 = 0.1\times10^{-3}$ m and $d_2 = 0.4\times10^{-3}$ m, and beam waist $\omega_0 = 80\lambda$. In this case, the orbital angular momentum is set to $\ell = 1$. (For interpretation of the references to color in this figure legend, the reader is referred to the web version of this article.)

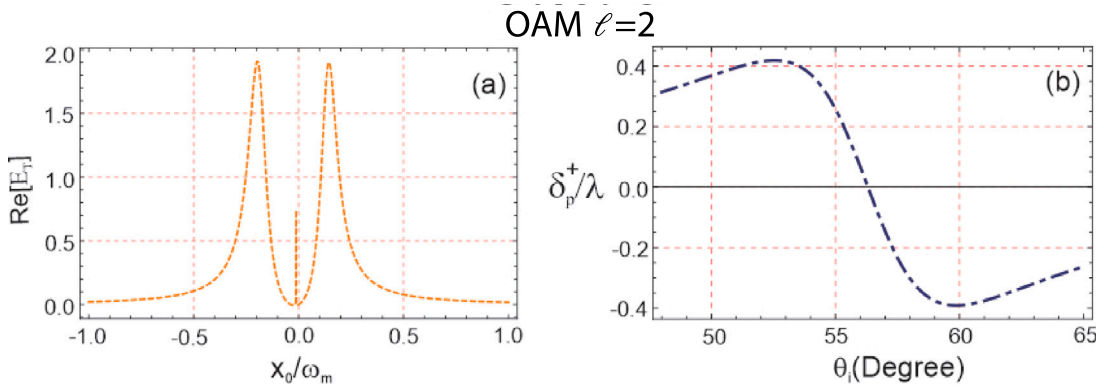

Fig. 4. (a) The dashed curve illustrates the absorption profile of the intracavity rovibrational system as a function of the normalized probe field detuning x_0/ω_m. Scaling relation for the detuning parameter: $\delta = x_0\omega_m + \omega_m$. This scaling is used to define the zero reference point for $\delta = \omega_b$. The parameters employed in the simulation are: mechanical oscillator mass $m = 0.8\times10^{-6}$ kg, cavity length $L = 0.005$ m, radius of the rotating mirror $R = 0.16\times10^{-6}$ m, input laser power $p_l = 6\times10^{-3}$ W, wavelength of probe field $\lambda = 22.7$ mm, optical decay rate $\kappa = \omega_\phi/10$, and mechanical and rotational frequencies $\omega_m = 5.7\times10^6$ Hz and $\omega_\phi = 5.6\times10^6$ Hz, respectively. Both mechanical and rotational damping rates are taken as $\gamma_\phi = \gamma_m = 0.00014$ Hz. In all scenarios, the orbital angular momentum is fixed at $\ell = 2$. (b) The normalized photonic SHE shift δ_p^+/λ is shown as a function of the incident angle θ for different probe detuning values. In this case, the detuning is set to $x_0 = -0.0415\,\omega_m$ (blue dot–dashed line), resulting in a clear displacement of the transparency window compared to the previous detuning of $x_0 = -0.01\,\omega_m$. The remaining parameters are held constant: $\epsilon_1 = \epsilon_3 = 2.22$, $\epsilon_2 = 1 + E_T$, with mirror thicknesses $d_1 = 0.1\times10^{-3}$ m and $d_2 = 0.4\times10^{-3}$ m, beam waist $\omega_0 = 80\lambda$. In this configuration, the orbital angular momentum is taken as $\ell = 2$. (For interpretation of the references to color in this figure legend, the reader is referred to the web version of this article.)

Fig. 3 examines the impact of non-zero OAM, setting $\ell = 1$ to activate rotational degrees of freedom in the intracavity optomechanical dynamics. Fig. 3(a) presents the absorption profile as a function of normalized detuning x_0/ω_m. Compared to Fig. 2, the inclusion of OAM qualitatively alters the optical response, generating a split transparency structure with two closely spaced minima. This splitting signals rovibrational mode hybridization, where the probe field couples simultaneously to vibrational and rotational motions of the cavity mirror, enabling additional destructive interference pathways.

Such a double-window structure is characteristic of rovibrational OMIT. The added rotational coupling reshapes the vibrational OMIT feature, introducing a secondary transparency window within the original dip and emphasizing the influence of OAM on cavity dynamics.

Fig. 3(b) shows the photonic SHE shift δ_p^+/λ as a function of incident angle θ, evaluated at probe detuning $x_0 = -0.0415\,\omega_m$. The dielectric layering remains the same as in Fig. 2.

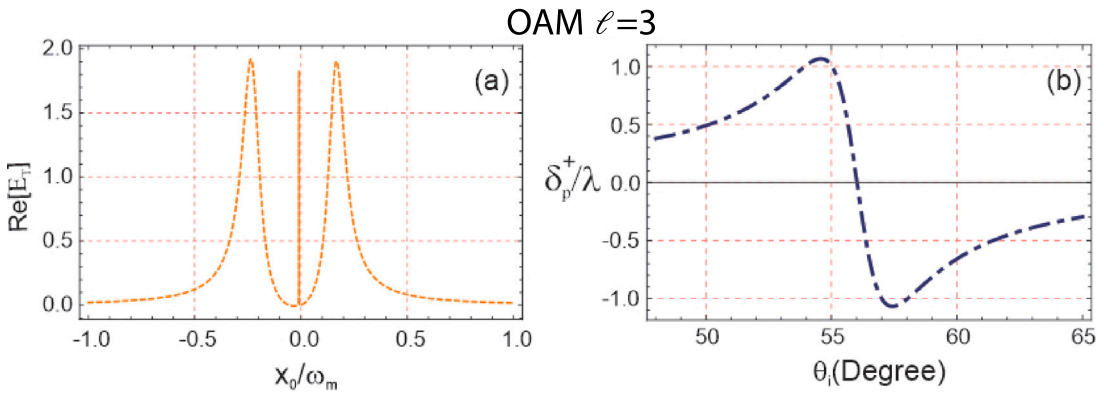

Fig. 5. (a) The dashed curve represents the absorption response of the intracavity rovibrational system as a function of the normalized detuning of the probe field, x_0/ω_m. Scaling relation for the detuning parameter: $\delta = x_0\omega_m + \omega_m$. This scaling is used to define the zero reference point for $\delta = \omega_b$. The system parameters used are: mechanical oscillator mass $m = 0.8 \times 10^{-6}$ kg, cavity length $L = 0.005$ m, rotating mirror radius $R = 0.16 \times 10^{-6}$ m, input laser power $p_l = 6 \times 10^{-3}$ W, wavelength of probe field $\lambda = 22.7$ mm, optical decay rate $\kappa = \omega_\phi/10$, and the mechanical and rotational mode frequencies $\omega_m = 5.7 \times 10^6$ Hz and $\omega_\phi = 5.6 \times 10^6$ Hz, respectively. The mechanical and rotational damping rates are $\gamma_\phi = \gamma_m = 0.00014$ Hz. Throughout this analysis, the orbital angular momentum is fixed at $\ell = 3$. (b) The normalized photonic SHE displacement δ_p^+/λ is plotted against the incidence angle θ for varying probe field detunings. In this configuration, the probe detuning is set to $x_0 = -0.0415\,\omega_m$ (blue dot–dashed curve), which causes a clear shift in the transparency window relative to the previously analyzed case with $x_0 = -0.01\,\omega_m$. All other parameters are kept the same: dielectric constants $\epsilon_1 = \epsilon_3 = 2.22$, $\epsilon_2 = 1 + E_T$, and mirror layer thicknesses $d_1 = 0.1 \times 10^{-3}$ m and $d_2 = 0.4 \times 10^{-3}$ m, beam waist $\omega_0 = 80\lambda$. In this case, the orbital angular momentum is taken as $\ell = 3$. (For interpretation of the references to color in this figure legend, the reader is referred to the web version of this article.)

Relative to the $\ell = 0$ case, the photonic SHE shift is noticeably diminished, with the lateral beam deflection falling short of the previously observed ±40 amplitude. This reduction arises from the emergence of dual transparency windows, which smooth out the refractive index gradient and weaken the sharp phase dispersion necessary for strong photonic SHE effects. Furthermore, the introduction of OAM modifies the intracavity field distribution through angular momentum exchange, thereby reducing the transverse phase asymmetry required for efficient spin–orbit interaction.

Altogether, Fig. 3 demonstrates that while OAM enhances spectral richness via rovibrational coupling, it concurrently weakens the photonic SHE response. This trade-off becomes particularly relevant for applications requiring spin-selective beam steering or phase-sensitive detection. The added rotational complexity improves spectral resolution but reduces the phase steepness near transparency, limiting photonic SHE efficiency. Optimizing such hybrid systems therefore requires careful balancing of OAM strength with dispersion characteristics. This insight provides a valuable design principle for integrated photonic platforms aiming to leverage both OMIT and spin–orbit phenomena.

Fig. 4 investigates the optical behavior of the intracavity rovibrational system under the action of enhanced OAM, specifically $\ell = 2$. This scenario enables exploration of how rotational dynamics modulate both the probe absorption spectrum and the photonic SHE.

In Fig. 4(a), the absorption spectrum (dashed line) is plotted against the normalized detuning x_0/ω_m. Compared to the earlier cases of $\ell = 0$ and $\ell = 1$ (Figs. 2 and 3), the spectrum now displays a broadened transparency region. More importantly, the emergence of two well-separated transparency dips indicates a stronger mode splitting, which is a direct consequence of increased torque-induced optomechanical coupling. The higher OAM enhances the angular momentum exchange between the rotating mirror and the optical field, thereby amplifying the interaction strength between rotational and vibrational modes. This dual-transparency signature suggests that the system supports multiple pathways for destructive interference, mediated by both rotational and vibrational resonances. The presence of multiple hybrid modes points to a higher degree of coherence and controllable optical interference enabled by structured light with non-zero OAM.

Fig. 4(b) shows the variation of the normalized photonic SHE shift, δ_p^+/λ, with the angle of incidence θ, for a fixed probe detuning of $x_0 = -0.0415\,\omega_m$. Despite the broader and more structured absorption response, the photonic SHE shift remains relatively weak. This reduction in magnitude—especially when compared with the $\ell = 0$ case—can be attributed to the smoother phase gradient near each transparency window. Although the windows are broader, the accompanying phase dispersion lacks the sharpness necessary for inducing strong spin-dependent splitting.

Additionally, the spatial energy distribution of the structured optical field at $\ell = 2$ may lead to reduced overlap with the spin-coupled regions at the dielectric interface. This redistribution limits the spin–orbit interaction, resulting in a diminished photonic SHE response.

Overall, increasing the OAM to $\ell = 2$ enhances spectral transparency by enabling stronger rovibrational coupling and mode hybridization, but the photonic SHE remains suppressed due to insufficient phase steepness and weaker interface interaction.

Fig. 5 continues this investigation for $\ell = 3$, where the impact of higher-order angular momentum on both optical absorption and spin–orbit coupling becomes more pronounced. In Fig. 5(a), the absorption spectrum is plotted as a function of normalized detuning x_0/ω_m. Compared to previous cases, the central transparency region becomes deeper and more defined, with clearly resolved dual

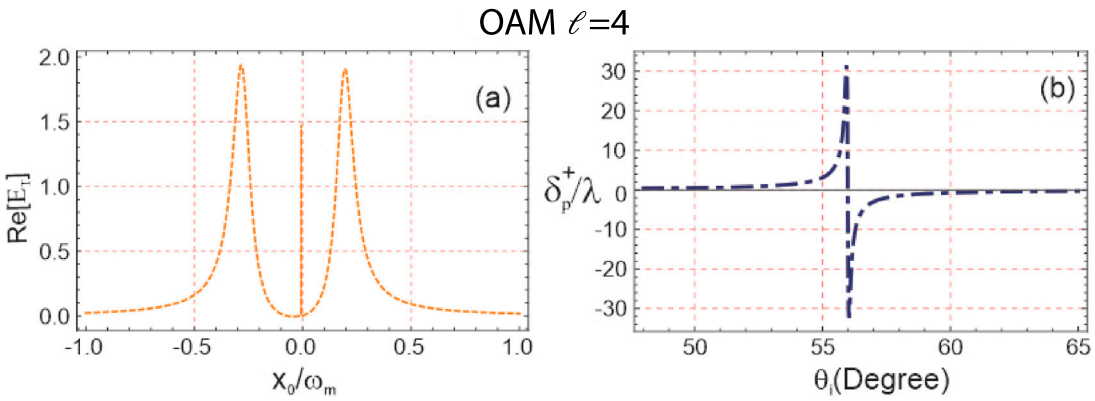

Fig. 6. (a) The dashed curve illustrates the absorption profile of the intracavity rovibrational system as a function of the normalized probe field detuning, x_0/ω_m. Scaling relation for the detuning parameter: $\delta = x_0\omega_m + \omega_m$. This scaling is used to define the zero reference point for $\delta = \omega_b$. The parameters used in the simulation are as follows: mechanical oscillator mass $m = 0.8 \times 10^{-6}$ kg, cavity length $L = 0.005$ m, radius of the rotating mirror $R = 0.16 \times 10^{-6}$ m, laser power $p_l = 6 \times 10^{-3}$ W, wavelength of probe field $\lambda = 22.7$ mm, optical decay rate $\kappa = \omega_\phi/10$, and mechanical and rotational mode frequencies $\omega_m = 5.7 \times 10^6$ Hz and $\omega_\phi = 5.6 \times 10^6$ Hz, respectively. The mechanical and rotational damping rates are set to $\gamma_\phi = \gamma_m = 0.00014$ Hz. In this analysis, the orbital angular momentum is fixed at $\ell = 4$. (b) The normalized photonic SHE shift, δ_p^+/λ, is depicted as a function of the incidence angle θ for distinct values of the probe field detuning. Here, the detuning is tuned to $x_0 = -0.0415\,\omega_m$ (blue dot–dashed curve), resulting in a noticeable displacement of the transparency window compared to the earlier case with $x_0 = -0.01\,\omega_m$. All other parameters remain unchanged: dielectric constants $\epsilon_1 = \epsilon_3 = 2.22$, $\epsilon_2 = 1 + E_T$, and mirror thicknesses $d_1 = 0.1 \times 10^{-3}$ m and $d_2 = 0.4 \times 10^{-3}$ m, beam waist $\omega_0 = 80\lambda$. For this plot, the orbital angular momentum is chosen as $\ell = 4$. (For interpretation of the references to color in this figure legend, the reader is referred to the web version of this article.)

transparency windows. This spectral refinement stems from intensified optomechanical interaction facilitated by increased torque and stronger angular momentum transfer between the rotating cavity mirror and the intracavity field.

The more prominent central dip is indicative of enhanced destructive interference among the hybridized optical and mechanical modes. This supports the hypothesis that structured light with higher OAM not only couples more efficiently to rotational degrees of freedom but also improves spectral tunability and coherence control within the system.

In Fig. 5(b), the normalized photonic SHE shift δ_p^+/λ is shown as a function of incidence angle θ, again at a fixed detuning of $x_0 = -0.0415\,\omega_m$. While the overall photonic SHE shift remains modest, a clear improvement is observed relative to the $\ell = 1$ and $\ell = 2$ scenarios. This enhancement arises from the steeper phase dispersion near the broadened transparency windows, which facilitates stronger lateral separation of spin components through the spin–orbit interaction mechanism.

Thus, for $\ell = 3$, the system exhibits dual and deeper transparency features along with a moderately amplified photonic SHE signal. The higher OAM contributes to both spectral refinement and better phase control, underscoring its utility as a powerful tuning knob in cavity-based optomechanical systems.

In summary, the results of Figs. 4 and 5 reveal that increasing the OAM strengthens optomechanical coupling, enriches the absorption spectrum with multiple transparency windows, and modulates the photonic SHE. While the photonic SHE shift does not scale linearly with OAM, its enhancement at higher ℓ demonstrates the critical role of phase dispersion and field localization in mediating spin–orbit interactions.

Fig. 6 presents the optical absorption characteristics and photonic SHE behavior for the intracavity rovibrational system under the influence of OAM $\ell = 4$. Fig. 6(a) displays the absorption spectrum (dashed curve) as a function of the normalized probe field detuning x_0/ω_m. In this regime, the system exhibits two transparency windows: one that is significantly broadened and another that remains relatively narrow. The broader window signifies enhanced destructive interference between the cavity and rovibrational sidebands, a direct consequence of the stronger light–angular momentum interaction introduced by the increased OAM.

This spectral reshaping indicates that higher-order OAM components promote asymmetry in the transparency profile, possibly due to the more intricate coupling dynamics between optical, mechanical, and rotational modes. Such control over the width and position of transparency windows is crucial for applications in tunable slow light and precision spectroscopy.

Fig. 6(b) illustrates the normalized photonic SHE shift δ_p^+/λ as a function of the incident angle θ, evaluated at the probe detuning $x_0 = -0.0415\,\omega_m$ (blue dot–dashed curve). Notably, a significant enhancement in the photonic SHE shift is observed at the location corresponding to the broader transparency window. The shift reaches a magnitude of approximately ± 35, which is a substantial increase compared to previous cases with $\ell = 1$, 2, and 3.

This enhancement confirms a stronger spin–orbit coupling induced by the higher OAM. The broadened transparency window corresponds to a steeper dispersion profile, which leads to an increased phase gradient and thus a larger transverse displacement between opposite spin components of the probe beam. Such a pronounced spin splitting is a hallmark of enhanced photonic SHE and could be exploited for spin-controlled light steering and high-resolution optical sensing. As a result, for $\ell = 4$, the system develops an asymmetric dual-transparency structure, with one broader and one narrower window. Simultaneously, the photonic SHE shift experiences a substantial amplification at the broader window, demonstrating the pivotal role of OAM in enhancing spin–orbit interaction in hybrid optomechanical platforms.

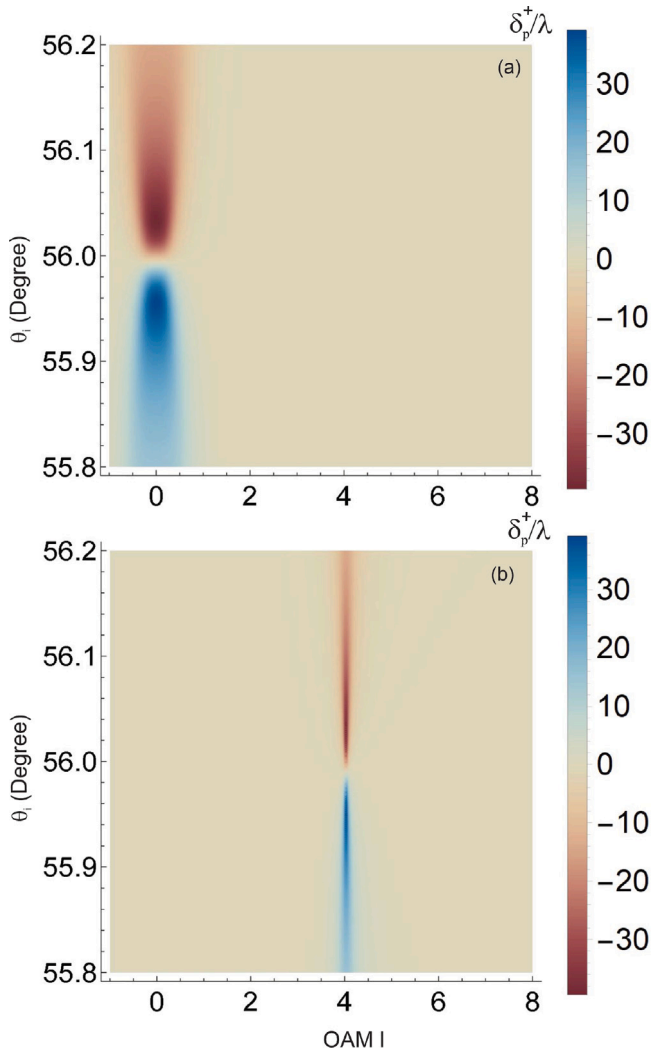

Fig. 7. Density plot of the normalized photonic SHE shift, δ_p^+/λ, as a function of the incident angle θ and the orbital angular momentum ℓ, for two probe field detunings: (a) $x_0 = -0.01\omega_m$ and (b) $x_0 = -0.0415\omega_m$. Other parameters are mechanical oscillator mass $m = 0.8 \times 10^{-6}$ kg, cavity length $L = 0.005$ m, radius of the rotating mirror $R = 0.16 \times 10^{-6}$ m, laser power $p_l = 6 \times 10^{-3}$ W, wavelength of probe field $\lambda = 22.7$ mm, optical decay rate $\kappa = \omega_\phi/10$, and mechanical and rotational mode frequencies $\omega_m = 5.7 \times 10^6$ Hz and $\omega_\phi = 5.6 \times 10^6$ Hz, respectively. The mechanical and rotational damping rates are set to $\gamma_\phi = \gamma_m = 0.00014$ Hz, $\epsilon_1 = \epsilon_3 = 2.22$, $\epsilon_2 = 1 + E_T$, and mirror thicknesses $d_1 = 0.1 \times 10^{-3}$ m and $d_2 = 0.4 \times 10^{-3}$ m, beam waist $\omega_0 = 80\lambda$.

Fig. 7 presents the density plots of the normalized photonic SHE shift, δ_p^+/λ, as a function of the incident angle θ and the OAM index ℓ, under two distinct probe field detuning values: (a) $x_0 = -0.016\,\omega_m$ and (b) $x_0 = -0.0415\,\omega_m$. These results elucidate how structured light, modulated by OAM, governs spin–orbit interactions in the intracavity optomechanical system.

In Fig. 7(a), the photonic SHE shift is significantly pronounced at $\ell = 0$, with a distinct dip–peak pair symmetrically distributed around $\theta \approx 56°$. This prominent spin-dependent beam deflection arises due to a sharp phase dispersion near the EIT-like window in the absorption spectrum, which maximizes the transverse shift through enhanced spin–orbit coupling. As ℓ increases, the intensity of the photonic SHE rapidly diminishes, approaching negligible values beyond $\ell = 2$. This decay is attributed to a redistribution of the optical field intensity away from the center, thereby reducing its overlap with the dielectric interface where spin–orbit coupling is most efficient. Moreover, higher OAM states introduce additional angular momentum degrees of freedom, which dilute the spin–orbit interaction by transferring energy into rotational modes rather than lateral displacement.

Conversely, Fig. 7(b), corresponding to a slightly larger probe detuning, reveals a shifted and reshaped spin Hall response. Here, the maximum photonic SHE shift emerges around $\ell = 4$, with a relatively narrow angular range centered at $\theta \approx 56.1°$. This behavior suggests that under specific detuning conditions, higher OAM values can recover and even enhance the spin-dependent deflection. The recovery is due to the strengthened rotational–vibrational hybridization at this detuning, which sharpens the phase gradient of the reflected field and revives strong spin–orbit interaction. Importantly, the narrow angular confinement indicates improved angular resolution, making such configurations suitable for precision sensing applications.

The results shown in Fig. 7 highlight the intricate coupling between detuning, OAM, and spin–orbit interaction within the rovibrational cavity. Detuning modifies the resonance between the cavity modes and molecular rovibrational transitions, thereby influencing the strength of light–matter coupling. When OAM with azimuthal quantum number $l = 1$ is introduced, the photonic modes acquire an additional phase structure, resulting in mode splitting and redistribution of the local optical density of states. This redistribution affects the spin-dependent transverse shift characteristic of the photonic SHE. The spin orbit interactions, which governs the interaction between the photon's spin and its orbital degree of freedom, is therefore modulated by both detuning and OAM, leading to a tunable photonic SHE that manifests as spectral shifts and intensity variations in the cavity transmission. This demonstrates that the interplay of these parameters can be used to engineer photonic states with tailored spin–orbit properties.

Spin–orbit interaction and non-monotonic behavior of the photonic SHE

The non-monotonic variation of the photonic SHE with increasing OAM stems from the intricate interplay among spin–orbit coupling, phase dispersion, and the hybridization of rotational and vibrational mechanical modes within the optical cavity. When OAM is absent, the system exhibits strong OMIT accompanied by steep phase dispersion, leading to prominent spin-dependent transverse beam shifts. However, as a modest amount of OAM is introduced, the rotational symmetry of the cavity becomes active, but the associated phase gradient begins to flatten. This flattening diminishes the effectiveness of spin–orbit interactions, resulting in a noticeable reduction in the photonic SHE strength at intermediate OAM values. With further increase in OAM, rotational-vibrational hybridization becomes dominant. The hybridized modes give rise to new transparency features with enhanced phase dispersion under specific detuning. This amplifies the photonic SHE, depending on the handedness of the OAM and the probe-cavity detuning.

This non-monotonic trend is consistently observed across the entire parameter space explored in our study, and it reflects a rich interplay between spin, OAM, and optomechanical coupling dynamics. Importantly, the probe output maintains a Gaussian profile, confirming that photonic SHE modulation arises from internal cavity processes rather than from structural changes to the input beam. These findings demonstrate that OAM serves as a tunable degree of freedom for controlling spin–orbit phenomena in cavity systems. By leveraging rovibrational interactions and detuning, the system allows for fine-grained control over light–matter coupling and spin-polarized optical responses.

Experimental feasibility and challenges

This work presents a comprehensive theoretical and numerical investigation into the influence of OAM on the optical response of cavity-based rovibrational optomechanical systems. The results demonstrate the significant role of OAM in modulating phenomena such as OMIT and the photonic SHE, thereby providing a robust theoretical foundation for the design of dynamically reconfigurable photonic platforms. While the present study is theoretical, its experimental feasibility is supported by recent advances in cavity quantum electrodynamics and structured light manipulation. The generation and control of OAM-carrying beams have become experimentally accessible through the use of spatial light modulators, q-plates, and spiral phase plates [46,47]. For instance, high-quality spiral phase plates enabling precise vortex generation with specified topological charge have been demonstrated using reproducible molding techniques [46].

Additionally, high-finesse optical cavities integrated with vibrational media are becoming increasingly viable. Recent works [48,49] have shown that coupling vibrational and rotational degrees of freedom with cavity fields is within reach of current experimental setups, paving the way for realizing the proposed rovibrational optomechanical configurations. Nevertheless, several challenges must be addressed to translate these predictions into practical implementations. These include preserving coherence in rovibrational states, achieving high-precision mode-matching between OAM beams and cavity modes, and developing sensitive detection schemes for spin-dependent photonic displacements. Overcoming these technical hurdles is crucial for validating the theoretical model and advancing toward real-world applications.

Furthermore, the proposed framework offers a promising foundation for future investigations into nonlinear optical interactions and quantum optomechanical effects. Potential extensions include exploring OAM-assisted photon–phonon coupling in nonclassical regimes and implementing OAM-based protocols for quantum information processing. These directions could lead to multifunctional photonic systems that integrate OMIT and spin–orbit interactions for enhanced optical control and quantum device functionality.

Conclusion

In summary, we have explored how the inclusion of OAM fundamentally alters the optical behavior of an intracavity optomechanical system with rovibrational coupling. By varying the OAM of the probe field, we uncovered a transition from conventional OMIT to a rich structure of multiple transparency features, attributable to the activation and hybridization of rotational and vibrational modes. Our results demonstrate that the interplay between OAM and internal system dynamics can be harnessed to tailor light propagation and absorption characteristics in a highly controllable manner. Importantly, the study reveals that the photonic SHE in such systems is not linearly correlated with OAM strength; rather, it exhibits a nuanced dependence on detuning, dispersion gradients, and rotational-vibrational coupling. This highlights the potential of using OAM as a tunable control parameter to optimize spin-dependent beam steering.

Overall, this work establishes a versatile platform for dynamically reconfigurable photonic devices, where structured light plays a central role in modulating intracavity interactions. Future extensions could include the exploration of nonlinear regimes, quantum correlations under strong drive conditions, and integration with metasurfaces or chiral materials to further enhance spin–orbit photonic functionalities.

CRediT authorship contribution statement

Muqaddar Abbas: Writing – review & editing, Writing – original draft, Investigation, Data curation, Conceptualization. **Ghaisud Din:** Writing – review & editing, Visualization, Methodology, Formal analysis, Data curation. **Akhtar Munir:** Writing – review & editing, Validation, Methodology, Investigation, Formal analysis. **Hamid R. Hamedi:** Writing – review & editing, Validation, Investigation, Formal analysis, Conceptualization. **Pei Zhang:** Visualization, Validation, Supervision, Funding acquisition, Conceptualization.

Declaration of competing interest

The authors declare that they have no known competing financial interests or personal relationships that could have appeared to influence the work reported in this paper.

Acknowledgments

This work was supported by the National Natural Science Foundation of China (Grant No. 12174301), the Natural Science Basic Research Program of Shaanxi (Program No. 2023-JC-JQ-01), and the Fundamental Research Funds for the Central Universities.

Data availability

Data will be made available on request.

References

[1] Aspelmeyer M, Kippenberg TJ, Marquardt F. Rev Modern Phys 2014;86:1391.
[2] Agarwal GS, Huang S. Phys Rev A—At Mol Opt Phys 2010;81:041803.
[3] Huang S, Agarwal G. Phys Rev A—At Mol Opt Phys 2011;83:023823.
[4] Kippenberg TJ, Vahala KJ. Opt Express 2007;15:17172.
[5] Kippenberg TJ, Vahala KJ. Science 2008;321:1172.
[6] Marquardt F. Quantum machines: measurement and control of engineered quantum systems (les houches session XCVI). Oxford University Press 2014; 2011,
[7] Aspelmeyer M, Meystre P, Schwab K. Phys Today 2012;65:29.
[8] Weis S, Rivière R, Deléglise S, Gavartin E, Arcizet O, Schliesser A, et al. Science 2010;330:1520. http://dx.doi.org/10.1126/science.1195596.
[9] Xiong H, Si L-G, Zheng A-S, Yang X, Wu Y. Phys Rev A—At Mol Opt Phys 2012;86:013815.
[10] Lin Q, Rosenberg J, Chang D, Camacho R, Eichenfield M, Vahala KJ, et al. Nat Photonics 2010;4:236.
[11] Teufel JD, Li D, Allman MS, Cicak K, Sirois A, Whittaker JD, et al. Nature 2011;471:204.
[12] Safavi-Naeini AH, Alegre TM, Chan J, Eichenfield M, Winger M, Lin Q, et al. Nature 2011;472:69.
[13] Chang D, Safavi-Naeini AH, Hafezi M, Painter O. New J Phys 2011;13:023003.
[14] Agarwal G, Huang S. Phys Rev A—At Mol Opt Phys 2012;85:021801.
[15] Favero I, Karrai K. Nat Photonics 2009;3:201.
[16] Thompson J, Zwickl B, Jayich A, Marquardt F, Girvin S, Harris J. Nature 2008;452:72.
[17] Bhattacharya M, Meystre P. Phys Rev Lett 2007;99:073601.
[18] Bhattacharya M, Meystre P. Phys Rev Lett 2007;99:153603.
[19] Bhattacharya M, Giscard P-L, Meystre P. Phys Rev A—At Mol Opt Phys 2008;77:013827.
[20] Liu Y-M, Bai C-H, Wang D-Y, Wang T, Zheng M-H, Wang H-F, et al. Opt Express 2018;26:6143.
[21] Bhattacharya M, Giscard P-L, Meystre P. Phys Rev A—At Mol Opt Phys 2008;77:030303.
[22] Eggleston M, Godat T, Munro E, Alonso M, Shi H, Bhattacharya M. J Opt Soc Amer A 2013;30:2526.
[23] Valenzuela SO, Tinkham M. Nature 2006;442:176. http://dx.doi.org/10.1038/nature04937.
[24] Onoda M, Murakami S, Nagaosa N. Phys Rev Lett 2004;93:083901. http://dx.doi.org/10.1103/PhysRevLett.93.083901.
[25] Bliokh KY, Bliokh YP. Phys Rev Lett 2006;96:073903. http://dx.doi.org/10.1103/PhysRevLett.96.073903.
[26] Hosten O, Kwiat P. Science 2008;319:787. http://dx.doi.org/10.1126/science.115269.
[27] Cardano F, Marrucci L. Nat Photonics 2015;9:776. http://dx.doi.org/10.1038/nphoton.2015.232.
[28] Bliokh KY, Rodríguez-Fortuño FJ, Nori F, Zayats AV. Nat Photonics 2015;9:796. http://dx.doi.org/10.1038/nphoton.2015.201.
[29] Chen S, Zhou X, Mi C, Luo H, Wen S. Phys Rev A 2015;91:062105. http://dx.doi.org/10.1103/PhysRevA.91.062105.
[30] Cai L, Liu M, Chen S, Liu Y, Shu W, Luo H, et al. Phys Rev A 2017;95:013809. http://dx.doi.org/10.1103/PhysRevA.95.013809.
[31] Yu X, Wang X, Li Z, Zhao L, Zhou F, Qu J, et al. Nanophotonics 2021;10:3031.
[32] Xie B, Su G, Wang H-F, Liu F, Hu L, Yu S-Y, et al. Nat Commun 2020;11:3768.
[33] Wan R-G, Zubairy MS. Phys Rev A 2020;101:033837.
[34] Wu J, Zhang J, Zhu S, Agarwal GS. Opt Lett 2019;45:149.
[35] Waseem M, Shah M, Xianlong G. Phys Rev A 2024;110:033104.
[36] Abbas M, Din G, Hamedi HR, Zhang P. Phys Rev A 2025;111:053716.
[37] Born M, Wolf E, Bhatia AB, Clemmow P, Gabor D, Stokes A, et al. In: Principles of optics: electromagnetic theory of propagation, interference and diffraction of light, vol. 7, Cambridge: Cambridge University Press; 1999.
[38] Wu L, Chu H-S, Koh WS, Li E-P. Opt Express 2010;18:14395, https://api.semanticscholar.org/CorpusID:23466980.
[39] Wu L, Chu HS, Koh WS, Li EP. Opt Express 2010;18:14395. http://dx.doi.org/10.1364/OE.18.014395.
[40] Xiang Y, Jiang X, You Q, Guo J, Dai X. Photon Res 2017;5:467. http://dx.doi.org/10.1364/PRJ.5.000467.
[41] Wan R-G, Zubairy MS. Phys Rev A 2020;101:033837. http://dx.doi.org/10.1103/PhysRevA.101.033837.
[42] Walls D, Milburn GJ. Quantum optics. Springer; 2008, p. 307–46.
[43] Peng J-X, Chen Z, Yuan Q-Z, Feng X-L. Phys Lett A 2020;384:126153.

[44] Gardiner CW, Zoller P. Quantum noise: a handbook of Markovian and non-Markovian quantum stochastic methods with applications to quantum optics. Springer Science & Business Media; 2004.
[45] Genes C, Vitali D, Tombesi P. Phys Rev A 2008;77:050307. http://dx.doi.org/10.1103/PhysRevA.77.050307.
[46] Oemrawsingh S, Van Houwelingen J, Eliel E, Woerdman J, Verstegen E, Kloosterboer J, et al. Appl Opt 2004;43:688.
[47] Massari M, Benassi A, Marinelli C, Bassi P. Appl Opt 2015;54:4077. http://dx.doi.org/10.1364/AO.54.004077.
[48] Shalabney A, George J, a. Hutchison J, Pupillo G, Genet C, Ebbesen TW. Nat Commun 2015;6:5981.
[49] Liao Q, Xu Q, Song M. Quantum Inf Process 2023;22:249.